The Effect of Magnetic Equilibrium on Auxiliary Heating Schemes and Fast Particle Confinement in Wendelstein 7-X

H. Patten[1], J.P. Graves[1], J. Faustin[2], W.A. Cooper[1], J. Geiger[2], D. Pfefferlé[3] and Y. Turkin[2]

[1]Swiss Plasma Center (SPC), École Polytechnique Fédérale de Lausanne (EPFL), CH-1015 Lausanne, Switzerland
[2]Max Planck Institute for Plasma Physics, Wendelsteinstraβe 1, 17491, Greifswald, Germany
[3]Princeton Plasma Physics Laboratory, Princeton 08540 NJ, USA

Abstract

The performance of the auxiliary heating systems Ion Cyclotron Resonance Heating and Neutral Beam Injection is calculated in three different magnetic mirror configurations foreseen to be used in future experiments in the Wendelstein 7-X stellarator: low, standard and high mirror. This numerical work is implemented with the SCENIC code package, which is designed to model three-dimensional magnetic equilibria whilst retaining effects such as anisotropy and the influence of including a Finite Orbit Width of the particles. The ability to simulate NBI deposition in three-dimensional equilibria, the implementation of the realistic beam injector geometry, and the modification of the SCENIC package to permit the investigation of the 3-ion species heating scheme, are recent developments. Using these modifications, an assessment of the advantages and disadvantages of these two fast-ion producing auxiliary heating systems is made in the three different magnetic mirror equilibria. For NBI heating, the high mirror configuration displays the best global confinement properties, resulting in a larger collisional power transfer to the background plasma. The standard mirror has the best particle confinement in the core region, but the worst towards the edge of the plasma. The low mirror has the largest lost power and thus the lowest total collisional power. For ICRH, the displacement of the RF-resonant surface significantly impacts the heating performance. Due to the large toroidal magnetic mirror in the high mirror equilibrium, resonant particles easily become trapped and cannot remain in resonance, generating only small energetic particle populations. Despite this, global confinement is still the strongest in this equilibrium. The low mirror is the only equilibrium to produce peaked on-axis collisional power deposition, with associated peaked on-axis fast ion pressure profiles. A highly energetic particle population is then produced but this results in larger lost power as this equilibrium is not sufficiently optimised for fast ion confinement. A comparison between the two heating methods concludes that NBI produces a smaller fraction of lost to input power, and a reduced sensitivity of the performance to variations of the toroidal magnetic mirror. The main limit of NBI which does not apply to ICRH is the production of highly energetic particle populations, with predictions of energetic particles of $E \sim 0.45MeV$.

1 Introduction

In the development towards a commercial nuclear fusion reactor, the stellarator concept could prove to be a promising design for a steady-state device. However, in order to progress to high perfomance plasmas, optimisation of the auxiliary heating sources is required. The fast-ion generating auxiliary heating systems to be used on the Wendelstein 7-X (W7-X) stellarator, Germany, are Ion Cyclotron Resonance Heating (ICRH) and Neutral Beam Injection (NBI). These two contrasting methods have very different influences on the production of the fast-ion population. ICRH predominantly increases the particle's magnetic moment [1] and the trapping fraction, whereas the anisotropic properties of NBI produced fast ions depend on the injection angle and the beam ionisation deposition. This seemingly small difference results in very different particle orbits and directly impacts the radial diffusion and confinement of such particles. In order to optimise these two heating systems, it is also necessary to evaluate the ability of the magnetic field configuration to confine these fast-ion populations. Flexibility of the magnetic topology is achieved via a modification of the individual modular coil currents. This then leads to very different

particle transport and plasma properties and therefore affects the overall performance [2].

The challenge of simulating the performance of NBI in W7-X has been recently attempted for modest values of $<\beta>=$ 2% [3, 4]. The NBI beam ionisation deposition was shown to be localised on the outer flux surfaces on the Low Field Side (LFS). Over slowing down timescales, large losses and high radial diffusion are predicted, and thermalised particles remain localised in the outer flux surfaces. Providing numerical insight into the performance of Ion Cyclotron Range of Frequency (ICRF)-wave and complicated magnetic geometry is extremely difficult and computationally expensive. Calculating the wave propagation with a fully localised antenna breaks the five-fold periodicity that is specific to W7-X. Simulations predicting the performance of minority species ICRH schemes in W7-X have been performed [5], where a comparison is made between two different magnetic topologies known as the 'standard' and 'high' mirror equilibria, (the difference between these is described in section 2.2). Due to the predominant perpendicular heating and large trapping fractions, poor confinement of resonant particles caused by ICRH was observed. Significant differences in the performance of ICRH in the high and moderate mirror equilibria were not observed (explained in section 2.2). The advanced ICRF heating scheme known as the '3-ion species' [6, 7] has also been previously explored in the high mirror equilibrium [8]. The results imply that despite developing a larger highly-energetic ion population than the minority heating scheme, the confinement of such particles is considerably worse due to increased radial excursion and reduced poloidal precession of particles among other reasons.

The aim of this paper is to explore the complicated interplay between magnetic toplogy and auxiliary heating schemes on fast ion production and confinement. The SCENIC [9] package includes a suite of several codes that permit the self consistent calculation of NBI and ICRF heating in two and three dimensional magnetic equilibria. The magnetic flux geometry is determined by the ANIMEC [10] code, including the anisotropic fast ion pressure contributions to the force balance equation. The generation of the neutral beam deposition fast ion population is performed using the VENUS NBI module [11], based on a realistic model of the three-dimensional NBI injector geometry. Calculation of the ICRF-wave propagation and absorption with a fully localised antenna is made using the LEMan [12] code. Finally, VENUS-LEVIS [13] is the Fokker Planck particle full- or guiding-centre motion following code. This includes the influence of Coulomb collisions with both energy and pitch angle scattering effects, and wave-particle resonant interactions via a Monte-Carlo based Quasi-Linear Operator (QLO).

The layout of this paper is as follows. In section 2, a simplified characterisation of the magnetic equilibrium parameters will be presented, including the influence of the equilibria on the particle guiding centre motion. Section 3 focuses on the roles of NBI heating on each of the magnetic topologies through particle deposition, radial diffusion and resultant slowing down distribution. Section 4 presents ICRH simulations with a focus on three-ion species heating [6], as well as the results from standard minority heating. Section 4 also includes an extensive study of the fast-ion distribution function and the influence of the resonance location on radial particle diffusion. The final section (5) compares the performance of the two fast ion heating methods. The total collisional power transferred to the background plasma and the lost power from the LCFS is calculated.

2 Magnetic Equilibria in W7-X

2.1 Simulation Profiles

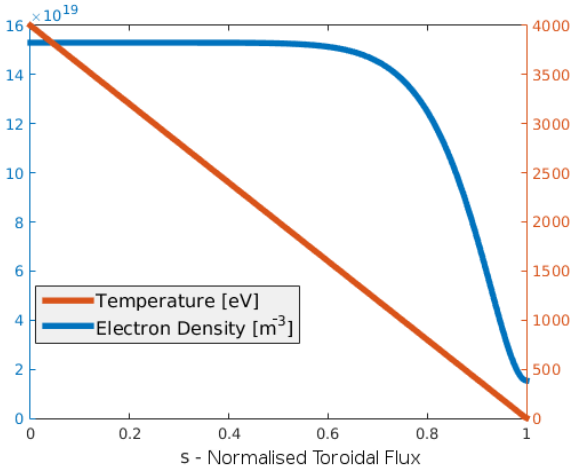

Figure 1: Background temperature and electron density profiles, with $s = \psi_{tor}/\psi_{tor,edge}$.

Within the first few campaigns, experiments at W7-X are likely to have a $\langle\beta\rangle$ value of between $2-3\%$. In these simulations, the global beta will be taken to be 3%, defined as:

$$\langle\beta\rangle = \frac{2\mu_0 \int p dV}{\int B^2 dV}. \quad (1)$$

The temperature profiles will be mostly imposed by the usage of Electron Cyclotron Resonance Heating

(ECRH) which is most efficient within the core, typically producing peaked temperature profiles. It is to be noted that the influence of ECRH cannot be simulated by the code package implemented in this work, though its influence will remain on the background temperature profiles and the ambipolar electric field described in section 2.3. To justify the plasma profiles chosen in the simulations presented in this paper, a few considerations are made. One of the benefits of stellarators is that no plasma current is required to produce the poloidal magnetic field, and therefore the Greenwald limit [14] does not formally exist for stellarators. This permits much higher densities to form, typically with a 'flat top' shape, as shown in figure 1. The electron density profile will be held fixed according to figure 1, and the temperature profile shown in figure 1 will be applied to all background plasma species. The assumption of $T_e \sim T_i$ is made to allow a comparison with the previous work of [3, 4] for which analytical profiles were also used. This assumption is also one of the aims of W7-X for future experimental campaigns.

Throughout the experiments that will take place over the first few years at W7-X, the number of neutrons produced during each shot is to be minimised. Therefore, it is foreseen that there will be no deuterium as the background plasma element during the commisioning and early use of ICRH. Due to this, the majority background plasma species in this paper has been chosen to be helium-4 in order to permit the use of certain Ion Cyclotron Resonance Heating (ICRH) schemes, to be described in section 4. The magnetic equilibria assumed in this paper are chosen so as to advance the work of [15]. In particular, we investigate configurations with low magnetic toroidal mirror and contrast the properties with the previously studied high mirror.

The individual currents in each of the modular coil sets are modified in order to produce different magnetic topologies using VMEC [16][1]. The equilibria are generated for a variety of different plasma $\langle\beta\rangle$ values, the Last Closed Flux Surface (LCFS) shape of which can be extracted. The LCFS used in the ANIMEC code [10] was taken from the free-boundary VMEC generated equilibria with zero plasma current radial profile.

2.2 Configurations with Varying Toroidal Magnetic Mirror

W7-X is a five-fold periodic stellarator. Changing the currents in each individual modular coil permits the creation of different magnetic equilibria, whereby one of the parameters often investigated is known as the toroidal magnetic mirror value, which refers to the relative strength of the toroidal variation of the magnetic field on the magnetic axis,

$$MR = \frac{B_{\varphi=0}(s=0) - B_{\varphi=\pi/5}(s=0)}{B_{\varphi=0}(s=0) + B_{\varphi=\pi/5}(s=0)}. \qquad (2)$$

Figure 2 compares the magnetic field strength along the magnetic axis for each magnetic topology over one period, encapsulating the bean section ($\varphi = 2n\pi/5$ with $n = 0, .., 4$) and the triangular section ($\varphi = (n+1)\pi/5$ with $n = 0, .., 4$).

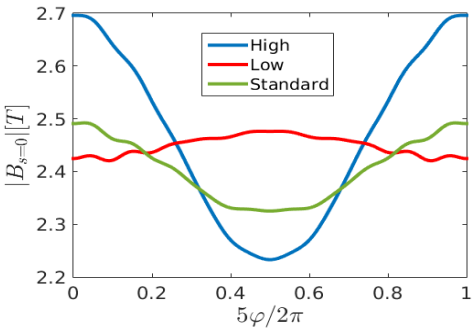

Figure 2: The magnetic field strength on axis against the toroidal boozer angle φ, for each magnetic configuration.

Representative parameters of equation 2 for high, low and moderate mirror equilibria are highlighted in table 1.

	MR %	max(B) [T]	min(B) [T]
High	9.4	3.14	2.14
Standard	3.5	2.95	2.22
Low	-0.8	2.92	2.28

Table 1: Comparison of some key values for the different magnetic equilibria investigated in this paper. Note that max(B) and min(B) are the maximum and minimum field values everywhere in the plasma (not at $\rho = 0$).

The High Mirror equilibrium is considered to be the best optimised ("advanced") magnetic topology for good reactor performance at high plasma beta, optimised for a range of parameters such as reducing bootstrap current, turbulent transport, divertor heating, etc. Low mirror is more like a classical stellarator where the magnetic field value along the magnetic axis is nearly constant for all toroidal angles.

[1]The free-boundary VMEC equilibria are available with EUROfusion access on the dedicated IPP data server

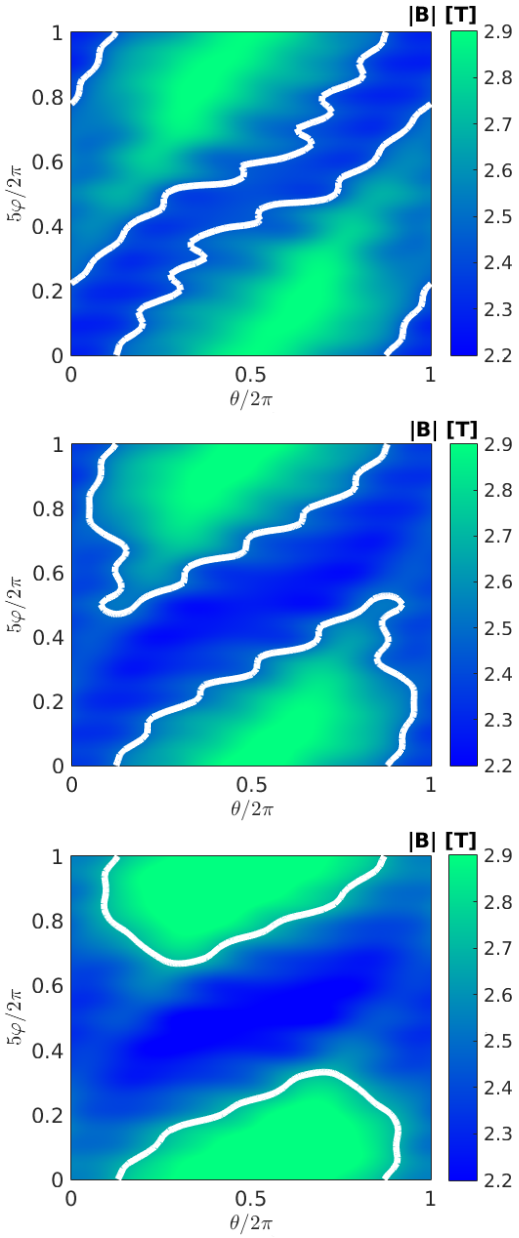

Figure 3: Plot of the magnetic field strength $|B|$ on the flux surface $\rho = \sqrt{\psi_{tor}/\psi_{tor,edge}} = 1.0$ for each of the different equilibria considered in this work: top) Low Mirror, middle) Standard Mirror and bottom) High Mirror, white line indicates the magnetic resonant surface to be described in section 4.

Figure 3 shows angular plots of $|B|$ at $\rho = 1$ for each of the three equilibria. Without the presence of Coulomb collisions or neoclassical plasma flows, particles with $B_{ref} = E/\mu < 2.4T$ in the low mirror equilibrium would precess toroidally over long time scales. However, for the High Mirror (bottom) most of these particles would be toroidally trapped and be subject to possible super-banana trajectories. As will be shown in sections 3 and 4, the role of the precession of particles in the toroidal and poloidal direction plays an important role in the confinement of trapped energetic particles in stellarator equilibria.

2.3 Ambipolar Electric Field Inclusion

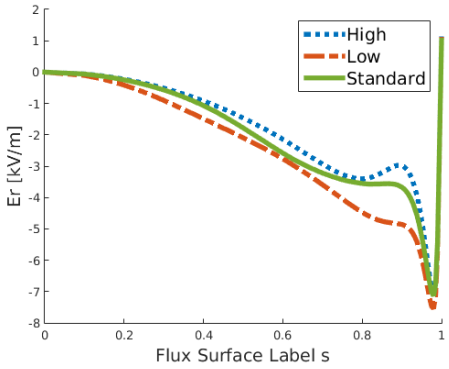

Figure 4: Radial electric field profiles calculated with the different magnetic geometries.

An ambipolar electric field is established in 3D configurations in order that average currents across flux surfaces vanish. These currents are generated by the differences in the radial transport between ions and electrons, which is smaller for electrons due to their smaller larmor radii. This therefore generates an ambipolar electric field to maintain quasineutrality, improving ion confinement. The magnitude of which is shown in figure 4. This field can be calculated through the following steps (described in [17]). The monoenergetic transport coefficients D_{ij}, as shown in [18], are obtained e.g. with the use of the DKES code [19]. With the inclusion of particle and heat source estimations as well as the ECCD current profile and other factors mentioned in [20], the radial electric field profiles then can be calculated. In order to ensure consistency for each of the three magnetic equilibria investigated in this paper, all of the same parameters and profiles were taken in order to produce the radial electric field profile $\mathbf{E_r}(\psi)$. Therefore, only the magnetic topology was a varied parameter for the calculation of $\mathbf{E_r}(\psi)$. The resulting fields are shown in figure 4 for each magnetic configuration. The influence of the ambipolar electric field is to induce both poloidal and toroidal plasma flows. The electric field affects the particle motions through the associated $\boldsymbol{E} \times \boldsymbol{B}$ particle velocity drift, which has components in only the poloidal and toroidal directions (i.e. no component across flux

surfaces):

$$\boldsymbol{v}_{\boldsymbol{E}\times\boldsymbol{B}} = \frac{\boldsymbol{E}\times\boldsymbol{b}}{B^*_{\|}} = \frac{E_r}{|\nabla s| B\sqrt{g} B^*_{\|}}(B_\theta \boldsymbol{e}_{\boldsymbol{\varphi}} - B_\varphi \boldsymbol{e}_{\boldsymbol{\theta}}). \quad (3)$$

Where B_θ and B_φ are the contravariant poloidal and toroidal magnetic field components directions respectively, $\boldsymbol{e}_{\boldsymbol{\theta}}$ and $\boldsymbol{e}_{\boldsymbol{\varphi}}$ are the unit vectors in the poloidal and toroidal directions respectively, $\sqrt{g}$ is the jacobian, ∇s is the gradient in the radial direction $s = \psi_\varphi/\psi_{\varphi,edge}$ and $B^*_{\|} = \boldsymbol{b}\cdot(\boldsymbol{B} + \rho_{\|}\boldsymbol{\nabla}\times\boldsymbol{B})$ is the modified magnetic field in the parallel direction. The ambipolar electric field has a differing influence on single particle motion in each of the magnetic equilibria, as shown in the example illucidated in figure 5.

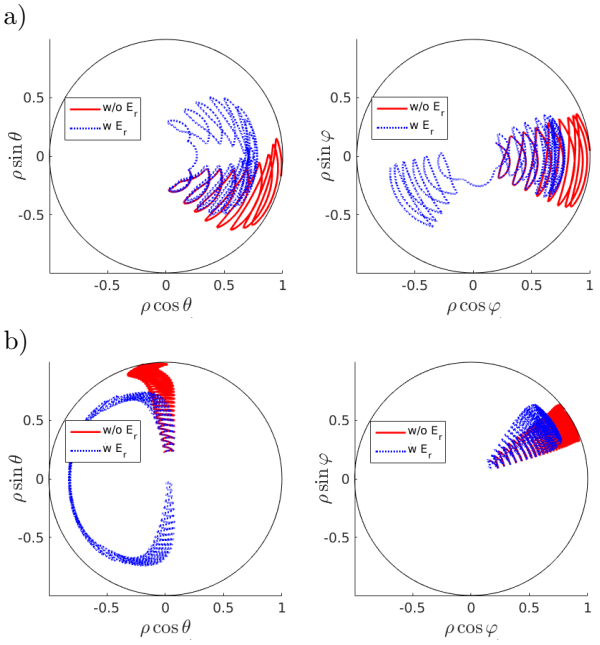

Figure 5: Examples of the contrasting influence of the ambipolar electric field on particle confinements for a) low mirror, b) high mirror. Plotted on the left over the poloidal (pseudo) plane, and the right the toroidal (pseudo) plane.

The particle orbits shown in figure 5 are calculated without the presence of Coulomb collisions for particles with a thermal energy $E = 4keV$ and a pitch angle $\lambda = 0.3$. In the high mirror equilibrium (b) the induced poloidal motion from the electric field plays an important role in the particles confinement. The toroidally induced motion in the high mirror does not significantly influence the confinement of the particle, since the strong toroidal magnetic well prevents toroidal period precession. In the low mirror equilibrium (a), particle confinement has been improved thanks to both the toroidal and poloidal motion generated by $\mathbf{E_r}(\psi)$. The high mirror case is consistent with earlier investigations into the influence of the amplitude of the radial electric field using VENUS-LEVIS (reference [21]). The results show that modifying the amplitude of the radial electric field profile by a large factor ($1-3$ times the original amplitude) does not strongly impact the number of lost particles from the plasma. The influence of the electric field was also shown to become less important for highly energetic particles. This is reflected by the general guiding-centre drift equations in general coordinates, solved by the VENUS-LEVIS code [13], and can be written in the simplified form [22]:

$$\dot{\boldsymbol{X}} = v_{\|}\frac{\boldsymbol{B}^*}{B^*_{||}} + \frac{\boldsymbol{E}^*\times\boldsymbol{b}}{B^*_{||}}, \quad (4)$$

$$\boldsymbol{E}^* = \boldsymbol{E} - \left(\frac{\mu}{q} + v_{\|}\rho_{\|}\right)\boldsymbol{\nabla}B - \rho_{\|}\dot{\boldsymbol{B}}, \quad (5)$$

$$\boldsymbol{B^*} = \boldsymbol{B} + \rho_{\|}\boldsymbol{\nabla}\times\boldsymbol{B}, \quad (6)$$

$$B^*_{||} = \boldsymbol{b}\cdot\boldsymbol{B}^*, \quad (7)$$

For highly energetic particles, the $\mathbf{E}\times\mathbf{B}$ drift in equation 7 will be much smaller than the magnetic drifts (first term in equation 7). Thus the influence of flows associated with $\mathbf{E}\cdot\nabla\rho$ will become negligible for particles with large energies relative to the amplitude of the radial electric field.

3 Neutral Beam Heating Modelling in W7-X

The deposition of the particles injected into a plasma can be calculated by a well known and simple equation for the beam deposition [23],

$$\frac{N_{beam}(l)}{N_{beam,0}} = e^{-\int_0^l n_e(l')\sigma_{eff}(l')dl'}. \quad (8)$$

Where l represents the line entering into the plasma from the NBI beam Positive Ion Neutral Injector (PINI) and σ_{eff} is the total cross section. This is a sum of the reactions that result in the deposition of a neutral particle: charge exchange and ionisation with background electrons and ions (including impurities). Resultingly, the beam deposition depends on the implementation of a realistic NBI geometry for each beam module as well as the plasma parameters such as density along the beam line and the plasma-neutral collision cross section σ_{eff}. In the neutral beam deposition module code VENUS-NBI [11], the collisional cross sections are calculated using the equations proposed in [24]. The equation used to calculate the charge exchange cross section is ~ 10 times larger than ionisation with electrons for

W7-X relevant densities and temperatures, given by

$$\sigma_{cx} = 0.6937 \cdot 10^{-18} \frac{(1 - 0.155 \cdot \log_{10} E)^2}{1 + 0.1112 \cdot 10^{-14} E^{3.3}}. \quad (9)$$

Here $E = W_b/m_b$ [eV/amu] is the beam injection energy normalised to the beam particle mass and σ has units m^2. The effects of the multistepping correction to σ_{eff} introduced by S. Suzuki, et al (1998) are also included. This is taken as $1.4 \cdot \sigma_{eff}$, corresponding to an electron density of $\sim 10e^{-20}$ and Zeff between $1 - 1.5$. The VENUS-LEVIS NBI module [11] has been recently updated to handle three-dimensional Last Closed Flux Surface (LCFS) geometries when calculating the entry and exit points of the beamline, previously having the capability for only axisymmetric systems. This is performed via the use of the method of volume pixelisation known as 'voxelisation' [25]. To calculate whether a test particle lies within the surface, a cubic grid is produced to encompass the entire structure. The injected beam particles are then binned into one of the small cubic elements. The LCFS shape is then discretised into triangular elements, and using basic planar equations between the surfaces of the cube with the surface of the triangles. Using this, an evaluation is made into whether a cube (a group of particles) exists within the plasma. Implementation of this update allows the study of NBI deposition in W7-X with realistic PINI geometry.

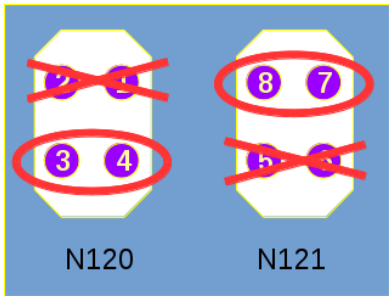

Figure 6: Labelling of the two NBI modules of W7-X, indicating which injectors have been used for the work presented in this paper in accordance with the setup for the first few experimental campaigns.

Currently two NBI modules are installed on W7-X: N120 and N121, each of which house four individual injectors. The location of these modules is as follows N120$(R, Z, \phi) = (6.750, -0.305, 0.993)$ and N121$(R, Z, \phi) = (6.750, 0.305, 1.520)$. Only two injectors per module have been used in the studies presented here, shown in figure 6, chosen according to what will be used within the first few experimental campaigns on W7-X. There are two slightly more tangential injectors, 4 and 8, at 1.78MW and two slightly more normal injectors, 3 and 7, at 1.64MW. The species power fraction for the hydrogen beam was set to 54.6%, 30.9% and 14.5% for the H, 2H and 3H neutral molecules respectively. The energy of the H beam particle is 55keV, with the 2H and 3H molecules resulting in a half and a third of the H energy respectively. The results were benchmarked successfully with other beam deposition codes such as BBNBI [26], NUBeam [27] and Beams3D [28].

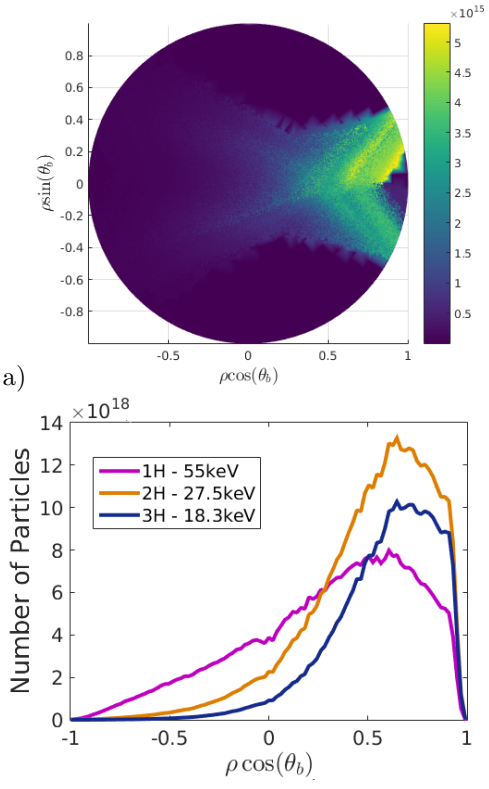

Figure 7: Number of particles produced from the neutral beam deposition for the standard mirror with $\langle\beta\rangle = 3\%$ a) plotted over two dimensions in a pseudo-cartesian coordinate system, distorting flux surfaces into concentric circles for visualisation, and b) deposition in the direction of the major radius for each of the hydrogen molecular ion components of the beam.

The use of the same density and temperature profiles for each magnetic equilibrium leads to similar neutral beam deposition profiles. The shine-through losses are predicted to be 10.63, 10.67 and 10.6% of the total injected particles for high, standard and low mirror respectively. Figure 7 illustrates the obvious problem with NBI as an auxiliary heating source for high beta 'flat-top' density profile plasmas, i.e. that the particle ionisation occurs at the edge, a result also found in [3]. The particles that penetrate into the core also tend to be those of higher velocity from the H_1 molecule, shown in figure 7 b). For reasonable core penetration of NBI

ions the density would have to be reduced to roughly $n_e \sim 0.25 \times 10^{20}$. This is reflected in figure 8. In contrast, W7-X has been optimised for high values of $\langle\beta\rangle$, thus for strong fusion performance this requires large plasma densities, resulting in outboard-edge localised deposition.

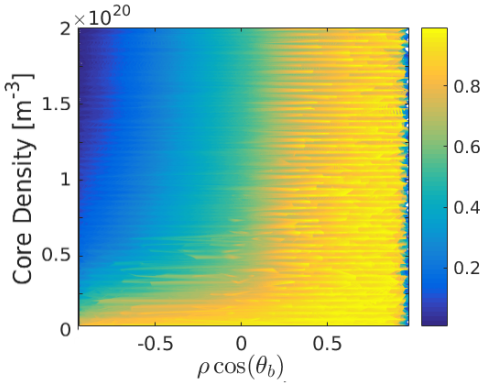

Figure 8: Number of particles produced by the neutral beam ionisation in the pseudo mid-plane direction whilst varying the core plasma background electron density. The colourbar values normalised according to the maximum in the number of particles per value of the electron density (#particles$|_{n_e}$)/ max(#particles$|_{n_e}$).

Good performance of a neutral beam heating system depends on the confinement of the beam ions and whether a substantial amount of energy of the beam ions can be transferred efficiently to the background plasma before the particle is lost from the system. As mentioned in the introduction, detailed work on the loss and diffusion of neutral beam particles has already been studied in references [3] and [4]. Further work will be presented here to make a comparison between the different magnetic topologies and also for a later comparison between Ion Cyclotron Resonance Heating and NBI heating. By utilising the guiding-centre following code VENUS-LEVIS [13], two different methods to simulate NBI particle behaviour have been investigated. In section 3.1 all markers are injected into the system at t=0, and are followed in order to investigate the confinement properties in the different magnetic topologies. In section 3.2, particles are constantly injected throughout the entire simulation in order to develop a realistic slowing down particle distribution.

3.1 Losses and Diffusion

The losses and radial diffusion of neutral beam particles can be investigated by recording the initial position of a particle and the position and time at which it reaches the last closed flux surface. This information enables calculation of the improved confinement time of NBI particles in the high mirror equilibrium relative to the low mirror case, as shown in figure 9. This figure also reflects the improved confinement of the beam particles at the edge of the standard mirror as compared to the low mirror equilibrium.

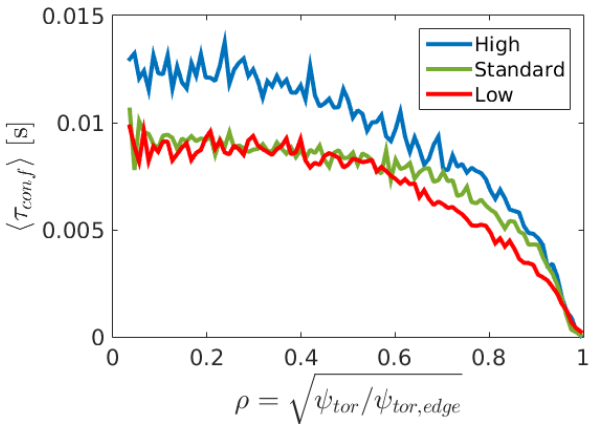

Figure 9: The confinement time of the particles plotted against the initial radial position, taken as the average of all the markers discretised in ρ, the radial flux surface label.

Evaluating the number of lost particles as a function of the toroidal position, shown in figure 10, this indicates the different loss mechanisms present in each case. The diffusive losses can be recognised as particles that are lost after $t \sim 5 \times 10^{-3}$s. Figures 10 (a) and (b) reflect these diffusive losses, whereby the x-axis has been normalised to extend over one toroidal field period. Figure 10 (b) represents the same simulations as (a) but without the presence of coulomb collisions. First and multiple orbit losses are particles lost before $t \sim 0.5 \times 10^{-3}$s. Figure 10 (c) illustrates these losses over 2π, as these losses only arise in specific toroidal locations. By comparison of figure 10 (a) and (b), it is seen that collisions act to 'kick' and therefore spread the particles to have less distinct loss regions. This behaviour arises via pitch angle scattering in the Monte-Carlo Coulomb collision operator, which is modelled in the VENUS-LEVIS [13] code. A comparison of figure 10 (a) and (b) illustrates that collisionality enhances particle losses as is known from neoclassical transport for stellarators [29,30]. For the low mirror configuration there are substantial losses at all toroidal locations, and for the high mirror the losses tend to be concentrated around the triangular sections of the stellarator.

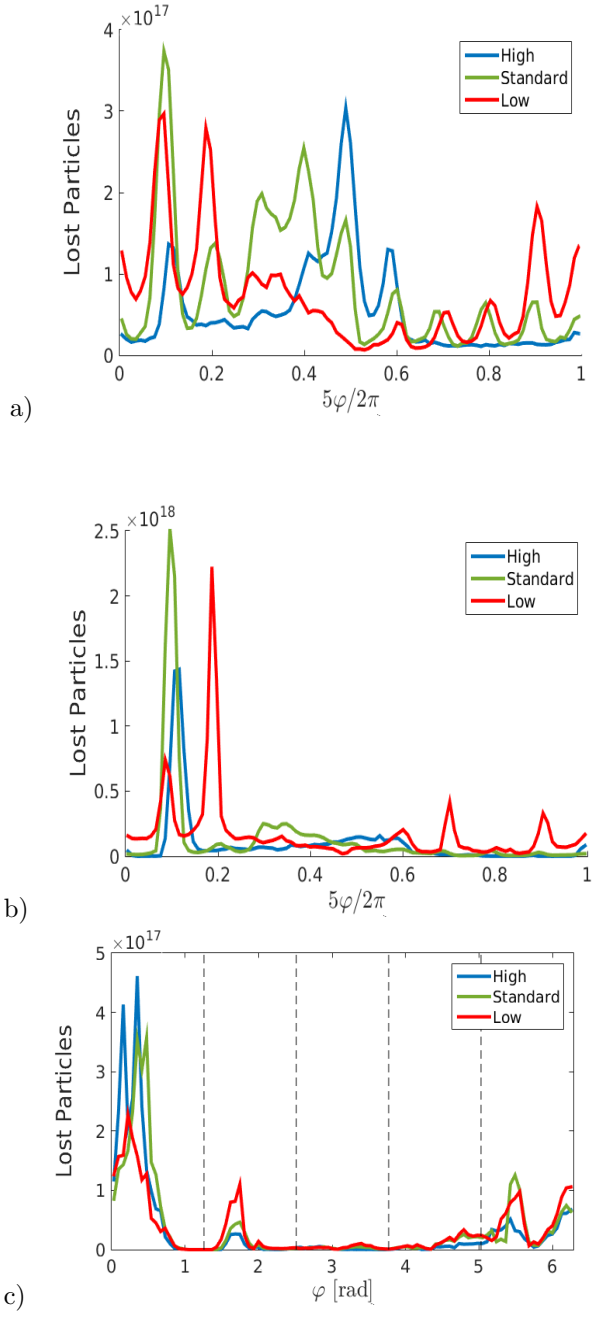

Figure 10: Neutral beam injected particle losses as a function of the toroidal angle, as the summation over all diffusive losses ($t > 5 \times 10^{-3}$s) in all toroidal periods for a) with and b) without Coulomb Collisions, and the period-localised first orbit losses ($t < 0.5 \times 10^{-3}$s). The vertical black lines in figure c) indicate the toroidal periods at the bean section.

In the collisionless simulations of figure 10(b), the standard mirror appears to have one distinct angle, $5\varphi/2\pi \sim 0.12$, where significant losses occur, most occuring at $5\varphi/2\pi \sim 0.12$. With the inclusion of coulomb collisions (figure 10(a)), the magnitude of this dominant toroidal loss channel is reduced compared to other peaks found at $5\varphi/2\pi \sim 0.33, 0.4$ or 0.47. Similar characteristics can be found in the low mirror equilibrium. In the high mirror equilibrium, the largest fundamental loss channel does not remain dominant like in the low or standard mirror, illustrating that trapped particles move into the magnetic well in the triangular section ($5\varphi/2\pi \sim 0.5$), away from the bean section ($5\varphi/2\pi \sim 0$), where they are then lost. First and multiple orbit losses shown in 10(c) have similar values for each equilibrium, with almost all losses found within the toroidal period of NBI injection or in the periods adjacent.

3.2 Slowing Down Distribution Function

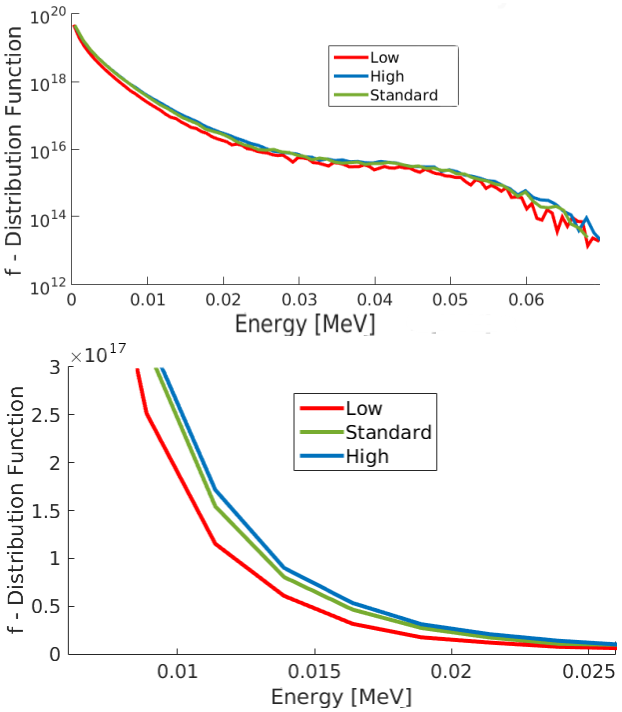

Figure 11: Slowing down beam energy distribution function for all NBI particles in linear-log space with a zoom into the energy region 6-25keV (linear-linear).

Taking the neutral beam deposition particle profile generated in section 3 and constantly injecting the markers throughout the simulation provides a prediction of the performance of NBI in experimental scenarios. A measure of this performance is the energy distribution of the beam ion population respectively via the length of the tail and the power transferred to the background species. The three magnetic configurations are com-

pared in figure 11a). Despite the improved particle confinement time of the high mirror in comparison with the other magnetic topologies, the number of highly energetic particles confined appears to be relatively similar between the equilibria.

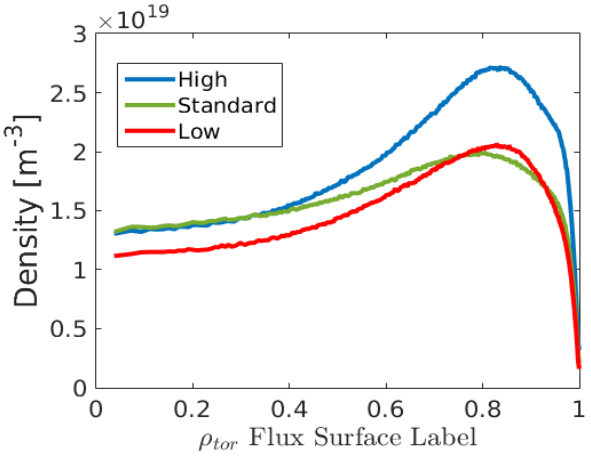

Figure 12: Edge localisation of the NBI particles, taken from the slowing down distribution.

Removing the log scale for the y axes shows that for $E = 20$keV, the high mirror confines almost twice the number of particles than the low mirror equilibrium, (see figure 11(b)). A reasonably substantial population of beam particles with $E \lesssim 50keV$ is maintained in the system for all magnetic equilibria. A table of lost NBI particles and power is given in table 2 in section 5.

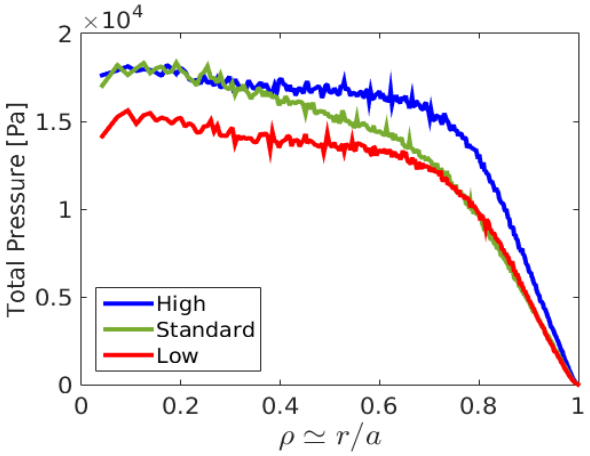

Figure 13: Total pressure from the NBI slowing down simulations.

While it is found that beam ions are confined up to reasonably high energies, the crucial issue is the edge localisation of the initial particle deposition. Continuous injection and collisions produce a slowing down distribution which remains peaked at the edge of the plasma, as indicated by the density, shown in figure 12. The total NBI pressure does not result in such edge localisation, as shown in figure 13, which is due to two main factors. The number of H_1 molecule particles ionised in the core compared to the H_2 and H_3 ionised at the edge, reflected by figure 7, combined with the peaked temperature profiles indicated in figure 1, leads to pressure profiles with maxima in the core region.

3.3 Summary of NBI Heating

The neutral beam ionisation code VENUS-NBI [11] has been updated to calculate the beam deposition in three dimensional geometries using the method of Voxelisation. Including the realistic geometry of the NBI injector geometry of W7-X allows the simulation of the fast ions injected into the system. Modifying the background plasma density, it has been shown that poor beam penetration to the plasma core is expected until the confinement becomes deoptimised (due to low electron density values), irrespective of the toroidal magnetic mirror value. Particles are ionised at the plasma edge, and even after slowing down timescales the particles are either lost or remain strongly edge localised. Evidence to explain the differences in performance of NBI in the different equilibria is found through studies of the lost particle populations. By considering the initial and final position of all the lost particles, it has been shown that the high mirror equilibrium has the largest average confinement time for all radial positions, followed by the standard mirror. The low mirror equilibrium has the largest radial diffusion and resultant losses. Simulating the beam ion motion with and without the influence of Coulomb collisions reveals the presence of different magnetic loss channels, which are specific to each magnetic mirror equilibrium. The loss channels remain distinct in the standard and low mirror even when collisions are induced, but the influence of collisions on the high mirror equilibrium acts to induce losses in the region of the toroidal magnetic well in the triangular section. The edge localisation of the beam particles poses a serious difficulty for the success of the NBI heating method, and therefore on the ability of W7-X to demonstrate relevant conditions to produce large numbers of fusion reactions.

4 Ion Cyclotron Resonance Heating

Two ICRF antenna's are foreseen to be installed on the W7-X stellarator [31]. The first to be commissioned

consists of two straps with a total power output of 1.5MW. The operational frequency range is 25-38MHz which permits on-axis fundamental heating of both hydrogen and helium-3 for plasmas with $B_0 \simeq 2.5T$. Simulations relevant to this antenna for various heating schemes will help to focus experiments, especially with regard to optimal magnetic configurations.

The strength of the ICRF wave-particle interaction strongly depends on two factors: the polarisation and the refractive index of the wave at the point of resonance. Polarisation refers to the relative strength of the electric field rotating in the direction of the ions compared to that of the electrons, which indicates the RF-heating transferred to the resonant ions.

$$\left|\frac{E_+}{E_-}\right|^2 \simeq \left(\frac{R - n_\parallel^2}{L - n_\parallel^2}\right)^2, \tag{10}$$

where, R and L are the right-hand and left-hand cut-offs respectively, explained in [32], and

$$E_+ = E_x - iE_y,$$

$$E_- = E_x + iE_y.$$

The role of R and L ensures that the polarisation of the wave depends not only on the charge to mass ratios of each species in the plasma, but also on the relative concentration of each species through the plasma frequency $\omega_{p,\alpha}$.

4.1 Resonant Surfaces

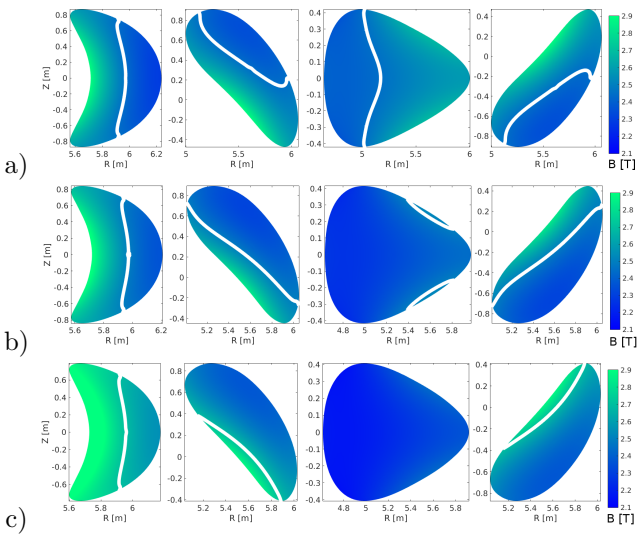

Figure 14: The magnetic field strength contours at the toroidal locations $\varphi = 0, \pi/10, \pi/5$ and $3\pi/10$

(from left to right) for the three different equilibria: a) Low, $B_{res} = 2.45T$, b) Standard, $B_{res} = 2.5T$ and c) High, $B_{res} = 2.7T$ with $B_{res} = m_\alpha \omega_{ant}/Z_\alpha e$. The white line indicates the resonant magnetic field value B_{res} for on-axis heating at the toroidal antenna position 6.7°.

The interaction between the ICRF-wave and a particle occurs when the following resonance condition is satisfied,

$$\omega = k_\parallel v_\parallel + n\Omega_{c,i}, \tag{11}$$

$$\Omega_{c,i} = \frac{Z_i e B}{m_i}.$$

n being the harmonic number of the cyclotron frequency. In the work presented here, only fundamental ($n = 1$) heating will be studied. Concerning equation 11, if the doppler shifted term ($k_\parallel v_\parallel$) is neglected, this implies that wave-particle energy exchange occurs on constant magnetic field contours. This absorption region is then broadened via the Doppler-shift-like effect. The RF antenna frequency used for the simulations was chosen such that the resonant interaction occurs on the magnetic axis at the same toroidal location as the ICRF antenna. For different toroidal positions, figure 14 illustrates the regions where particles receive energy from the wave: near to the white lines. The equilibrium toroidal magnetic mirror influences significantly the toroidal displacement of the resonance location. For the high mirror equilibrium, there are no possible means of efficient energy transfer near to the triangular toroidal section ($\varphi = \pi/5$). In contrast to this, the low mirror equilibrium permits strong on-axis resonance for all toroidal locations around the stellarator.

4.2 ICRF Heating Methods

One of the most commonly used ICRF heating methods is referred to as the 'minority species heating scheme', where a small concentration (roughly between 1-5%) of a minority species is added to the plasma. The advanced ICRF '3-ion species' heating scheme requires a plasma composed of two different majority species, and extremely small concentrations of a third minority species. Similarly to the minority species scheme, wave-particle resonance $n_\perp^2 < 0$ occurs in a region dictated by the charge mass ratio of the three species as well as the relative species concentrations. If the condition

$$(Z/A)_{M(1)} < (Z/A)_{min} < (Z/A)_{M(2)}. \tag{12}$$

is satisfied, then this resonance region is closely located to the 'L' cutoff layer, where

$$\left|\frac{E_+}{E_-}\right|^2 >> 1. \tag{13}$$

The polarisation is maximised in the absorption region if the concentration of the minority species is sufficiently low, permitting efficient ICRF-particle coupling. In this paper, a focus is made on the 3-ion species scheme performance, using the plasma concentrations X[H]=68%, X[4He]=15.9% and X[3He]=0.1%, the concentration defined as n_α/n_e to obey quasineutrality. The choice of this plasma species mixture is given by equation 8 in reference [6],

$$f^*_{M_1} \simeq \frac{\tilde{Z}_{min} - \tilde{Z}_{M_1}}{\tilde{Z}_{M_2} - \tilde{Z}_{M_1}} - \frac{(\tilde{Z}_{M_2} - \tilde{Z}_{min})(\tilde{Z}_{min} - \tilde{Z}_{M_1})}{\tilde{Z}_{M_2} - \tilde{Z}_{M_1}}\zeta, \tag{14}$$

where $\tilde{Z}_\alpha$ is the charge to mass ratio $(Z/A)_\alpha$ and ζ is related to plasma parameters such as the electron density, major radius and parallel wave number of the injected ICRH. A comparison is made with the standard minority heating scheme, investigating the performance of a minority concentration of X[H]=3% in a Helium-4 plasma background.

4.3 Fast Ion Pressure Distribution

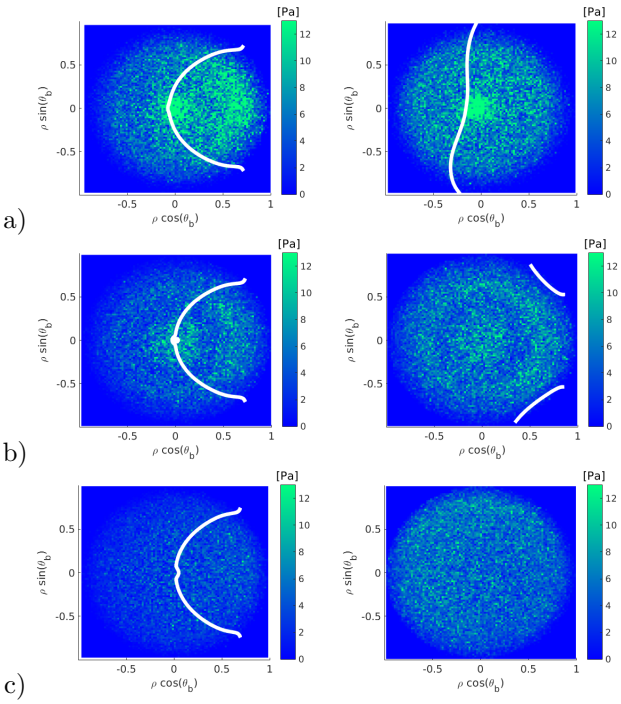

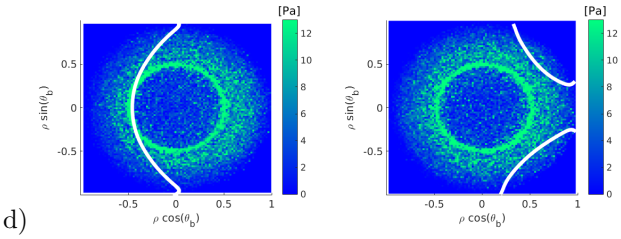

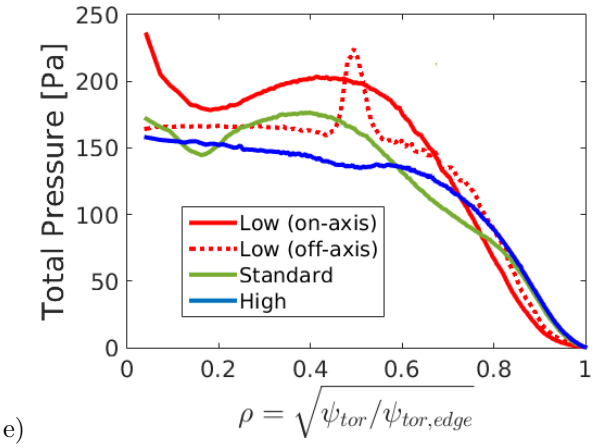

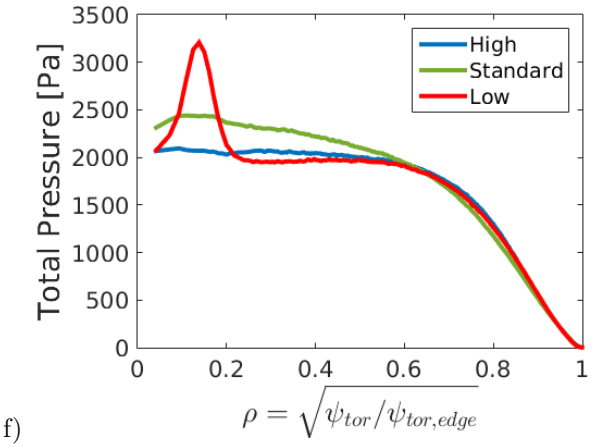

Figure 15: Fast ion ($v > 5v_{th}$) pressure plots for a) low, b) standard, c) high and d) HFS heating in the low mirror equilibria for the 3-ion species ICRH scheme. Left) Bean section $\varphi = 0 \pm 0.2$, right) triangular section $\varphi = \pi/5 \pm 0.2$. The white line indicates the line of resonance according to the B_{res} contour. The total 2D pressure is also given for the e) 3-ion species and f) minority heating schemes.

The comparison of the development of large fast ion pressures for the 3-ion species heating scheme is shown in figure 15, plotted as the summation of particles near to (± 0.2 rads) the bean and triangular (pseudo) poloidal planes. The separation of fast and thermalised particles was undertaken through a condition on the local (to the flux surface) thermal velocity $v > 5v_{th}$ at any given position in configuration space. Immediately noticable is

that the low mirror equilibrium generates considerably larger fast ion pressures than both the standard and high mirror cases. In addition to this, the pressure peaking on-axis is maintained even in the triangular toroidal section, away from the ICRF antenna. Pressure peaking associated with trapped particles can be seen in the bean section toroidal image (left) of the low mirror, since trapped particles align their bounce-tips with the resonant layer, a point further explained in section 4.4. Particularly interesting is that the fast-ion pressure peaks in the triangular toroidal section, rather than in the bean section where the RF-antenna is located. This is as a result of the toroidal particle trapping mechanism. The particles are heated in the perpendicular direction and the orbits then transition to become deeply trapped in the toroidal well between two bean periods. A comparison between the total pressure between the minority and 3-ion species heating schemes can be made between figures 15 e) and f). The larger concentrations used for the minority heating scheme (3%) evidently increases significantly the collisionality, making it difficult to generate energetic populations and thus pressure profiles that are not almost thermal. The values for the collisional power are given in tables 4 and 3 for the minority and 3-ion species heating schemes respectively. This agrees with the previous simulations that investigated minority heating in standard and high mirror equilibria [21].

4.4 ICRH-Modified Radial Diffusion

The Quasi-Linear Operator of VENUS-LEVIS [13] employed to simulate wave-particle interaction through a Monte-Carlo process utilises the perpendicular velocity diffusion coefficient [9]. This leads to an equation for the wave-particle 'kick' in the perpendicular direction. The Kennel-Engelmann constraint can then be applied to calculate the associated parallel wave-particle interaction.

$$v_{\perp}^2 + \left(v_{\parallel} - \frac{\omega}{k_{\parallel}} \right)^2 = const. \tag{15}$$

As described by T. Stix [1], this constraint naturally incorporates the physics that particles will align their bounce tips with the ICRF-resonant surface, a phenomena that applies to both tokamak and stellarator configurations. Investigating the influence of the resonant surface on the alignment of particle bounce tips, this section will focus on the radial particle diffusion and the associated losses. The total particle losses for the minority and 3-ion species heating schemes are given in tables 4 and 3. In the high mirror, particles do not interact significantly with the resonant surface. Once they interact with the RF-wave, they become trapped and move into the large toroidal magnetic well between two bean sections. The region of largest electric field amplitude is located close to the RF-antenna, which lies near the bean shape. Therefore, particles cannot easily remain in resonance with the wave before becoming trapped in regions of lower field amplitude. Evidence for this is reflected in the pressure peaking shown in figure 15 c), which indicates that the average pressure is highest in the triangular compared to the bean section, away from the RF-antenna. This phenomena is exhibited for both RF heating schemes.

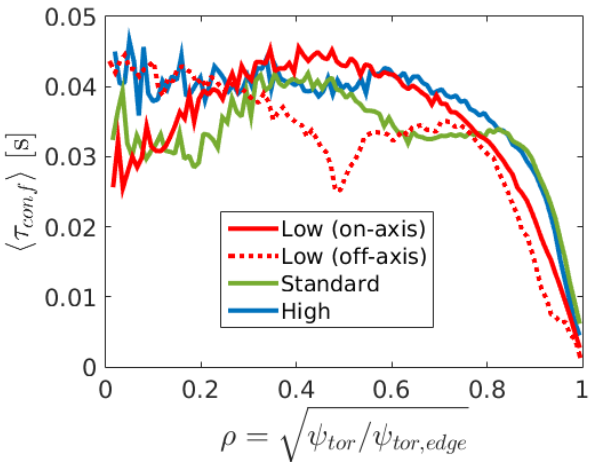

Figure 16: The confinement time of the energetic 3-ion species RF-heated particles plotted against the initial radial position, taken as the average of all the markers discretised in ρ (the radial flux surface label).

The constant value of the magnetic field strength in the low mirror configuration resembles that of a tokamak geometry. The on-axis 3-ion species simulation in the low mirror configuration indicates that resonant particles in the core tend to align their bounce tips close to the axis, leading to peaked density and pressure profiles (figures 17 a) and 15). This is a feature well known in tokamak geometries, linked to equation 15. However, the poor confinement of energetic particles in stellarator geometries leads to a reduced average confinement time in the region where energetic particle populations are being produced (figure 16). The standard mirror equilibrium displays behaviours from both the high and low mirror configurations. The fast ion pressure in the bean section in figure 15 b) left) shows the pressure induced by the trapped fast particle population present at outer flux surfaces $\rho \sim 0.4$, similar to the low mirror. However, the average fast ion pressure in the triangular section (figure 15 b) right)) is higher than that in the bean section, implying a toroidal trapping mechanism similar to the high mirror. The confinement time for the energetic 3-ion species heated particles is lower than

both the high and low mirror between $0.15 < \rho < 0.75$.

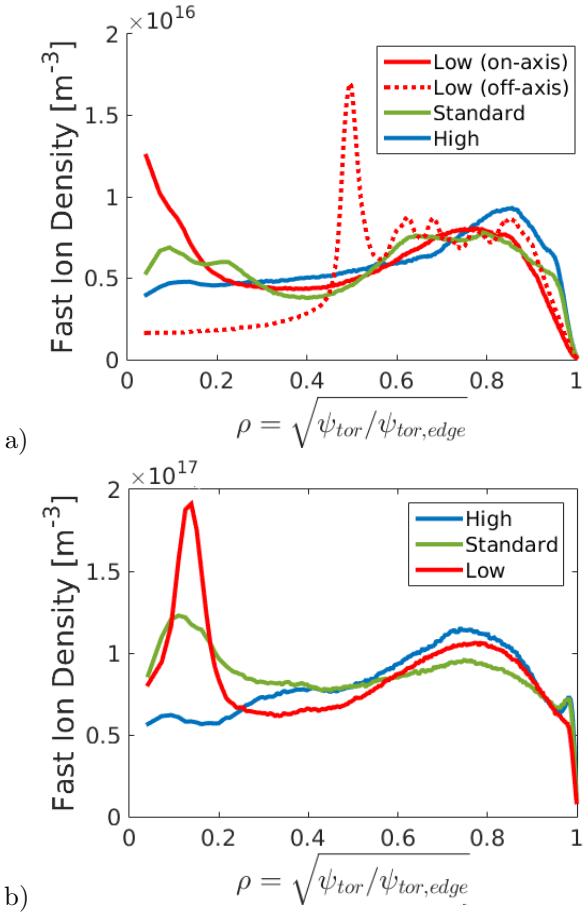

Figure 17: Fast ion ($v > 5v_{th}$) density plots for the a) 3-ion species and b) minority heating ICRF schemes, the dashed red line represents the off-axis low mirror simulation.

This can be explained by the radial shifting of the RF-resonant surface from figure 14. Resonant ions stick to this resonant surface and diffuse radially outwards until they cannot further interact with the wave. This differs from the high mirror case as the particles in the high toroidal magnetic mirror equilibrium interact with the RF-wave in many different regions of the plasma, preventing any observable pressure or density peaking. Comparing the difference between the production of fast ion populations in the standard and low mirror. Particles in the low mirror case at $\rho \sim 0.45$ (where the edge pressure peaks) have regions of the plasma where resonant interaction can occur for any toroidal angle. This produces a peaking in density and pressure associated to fast ion populations that exist in resonance with the wave. The differences between the 3-ion species and minority heating methods shown in figure 17 reveals the advantages of the minority heating method. Considering that minority heating consists of 3% and the former 0.1% concentrations of the background electron density, the total number of fast ion particles (continuing the definition $v > 5v_{th}$ as before) are relatively low for the minority heating scheme. The most significant difference in the fast ion densities produced with this method over that of the 3-ion species is reflected in the standard mirror equilibrium, which is edge localised for the 3-ion species but not for the minority heating scenario.

To further investigate the radial diffusion in the presence of ICRH, a simulation of off-axis (High Field Side - HFS) heating in the low mirror configuration with $B_{res} = 2.6T$ is shown in figure 15 d). The radial location where the particles tend to most strongly interact with the wave results in a pressure peaking of resonant particles at $\rho \sim 0.5$. Particles within the region $\rho < 0.45$ are mostly thermal, reflected by the reduced contribution to the fast ion density (figure 17 a)) and the collisional power transfer shown in figure 20 b). This also illustrates why the total pressure and confinement time (figures 15 and 16) within this same region are similar to the high mirror equilibrium. The off-axis low mirror simulation resulted in a total percentage loss of 18.7%, a value larger than on-axis simulations for all other equilibria. This is due to the production of highly energetic particles similar to those of the on-axis low mirror equilibrium (see figure 18 a)) but on outer flux surfaces, where particle confinement is reduced. The location of the RF-resonant surface with respect to the magnetic axis is concluded to have a large influence on the radial diffusion of resonant particles. This can be modified by the RF-antenna frequency or by the magnetic field strength.

4.5 ICRH Distribution Functions

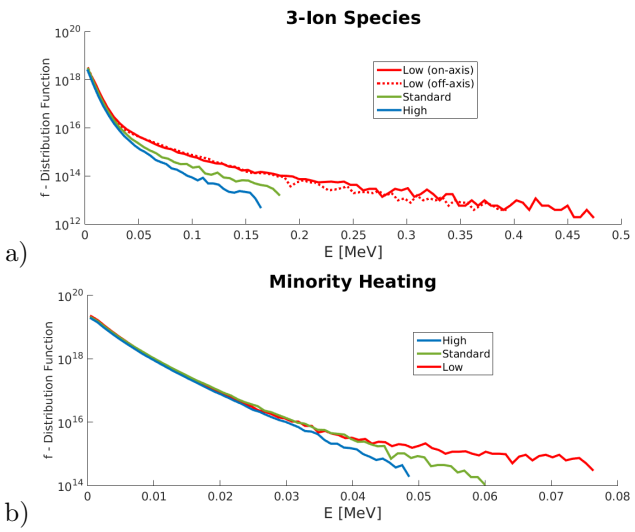

Figure 18: Comparison of the resultant distribution functions for a) the 3-ion species heating (including off-axis low mirror in dashed line) and b) minority heating for the different magnetic equilibria.

The resulting fast ion distribution functions for the advanced 3-ion species and minority heating schemes are shown in figure 18. Unlike the NBI slowing down distribution functions, it is evident that the highly energetic particle population is significantly influenced by the toroidal magnetic mirror amplitude using RF heating. Simulations of both on and off-axis heating in the low mirror equilibrium (figure 18 a)) reflect the improved performance compared to the high and standard equilibria for generating highly energetic ion populations, despite the lower confinement time of the highly energetic ions shown in figure 16. A table of the percentage of lost ICRH particles and power is given in tables 3 and 4 in section 5. Comparing the high and standard mirror, the standard mirror succeeds in producing more highly energetic ions above the energy $E > 0.05MeV$ for 3-ion species and $E > 0.03MeV$ for minority heating, despite the increase in lost particles.

4.6 Summary of ICRF Heating

The propagation of ICRF waves in 3D magnetic geometries was presented in section 4.1, illustrating the influence of the toroidal magnetic mirror effect on the displacement of the RF resonant surface. Additionally, with respect to the RF-antenna to be installed on W7-X for the OP2 experimental campaign, the main ICRF heating schemes applicable are the minority species and the 3-ion species heating schemes, explained in section 4.2. Focusing on the latter heating scenario, the results explain the influence of the presence of the ICRF resonant surface on confinement. The influence of ICRH to align the bounce tips of a particle with the resonant surface can have either a positive or a negative impact on the overall performance, due to the intricacies of the three-dimensional magnetic equilibrium used. For 3-ion species heating in the standard mirror case, the line of resonance - as shown in figure 14 - is radially displaced from the magnetic axis. When the particles align their bounce tips with this layer they are then radially displaced outwards into regions of reduced confinement. However, the increase in radial diffusion does not necessarily result in a reduced fast ion pressure or energetic distribution function. Illustrated in figures 18 a) and 15, the off-axis low mirror configuration also generates highly energetic particle populations and fast ion pressures. This is because the reduced displacement of the resonant surface - compared to the standard or high mirror - allows particles to remain in resonance, thus increase in energy, despite the larger total losses. The regions where highly energetic particles ($E > 0.01MeV$) are produced have also been shown (figure 16) to reduce the confinement time of particles within this region. The issues presented by the 3-ion species scheme are that fast ion density profiles have large concentrations on outer flux surfaces due to the trapped particle populations produced by ICRH. Additionally, the 3-ion species scheme is known to be difficult to implement in experiments due to the extremely low particle concentration requirements ($\sim 0.1\%$). The minority heating scheme, previously studied in [21] for the standard and high mirror equilibria, should not be used for experiments which aim to generate highly energetic particle populations. The larger collisionality than that of the three-ion species scheme makes it difficult to generate superthermal tails. However, use of the minority heating in the standard mirror succeeds in generating fast particle densities that are peaked on axis, which is not the case for the 3-ion species scheme. Using minority heating in the standard mirror, a peaked on-axis fast ion density is generated, but due to the larger concentration of particles no highly energetic particles are produced. This leads to fewer losses than for the 3-ion species method, shown in table 4. Minority heating in the standard mirror also generates 3.3 times less lost power than the low mirror, but at 0.72% (0.01MW), this is negligible compared to the 3-ion species scheme at 18.1% (0.27MW). The highly energetic particles produced by the 3-ion species scheme in the low mirror equilibrium could be used in experiments to replicate the behaviour and confinement of alpha particles, and to provide an insight into particle-Alfvén Eigenmode resonant interaction in W7-X.

5 Comparison of Heating Schemes

a)

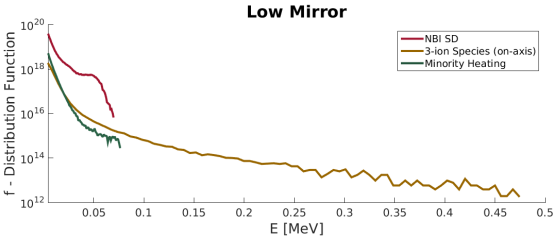

b)

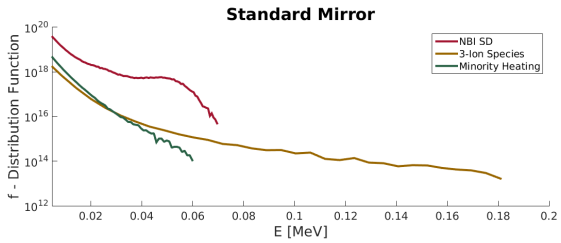

c)

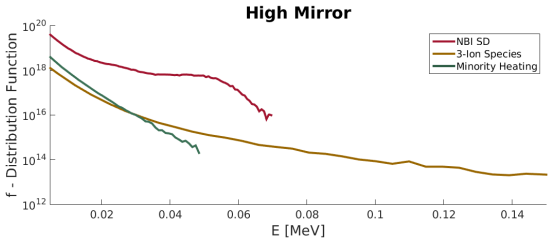

Figure 19: Comparison of the resultant distribution functions from NBI and ICRF heating, where both the ICRF minority heating and 3-ion species heating schemes have been included for the a) low , b) standard and c) high mirror equilibria. Noting different x-axis used for the low mirror case.

The resulting fast ion distribution functions for each of the heating schemes are presented in figure 19. With respect to the development of a large concentration of fast particles, the relative differences in the distribution functions for large energies is smaller for NBI heating when comparing all magnetic equilibria. Regarding the population of highly energetic fast ions, the 3-ion species outperforms the other heating schemes, especially for the low mirror magnetic geometry. Furthermore, for the minority heating scheme, only in the low mirror does the RF heating produce particles more energetic than from NBI. The heating transferred to the background plasma is reflected in the collisional and lost power. Tables 2 and 3 reflect the balance of the input-power with the two output power channels: the lost and collisional power. These three tables were calculated differently. For NBI heating, the two output powers were evaluated using all of the losses and collisions throughout the entire simulation, this means that the energy stored in the plasma is included in the total power. For ICRF heating, a state of numerical convergence in energy is first achieved and then the lost and collisional power is evaluated with the data obtained upon convergence and therefore neglects the energy stored in the plasma. Therefore, lost and collisional powers do not balance for NBI simulations due to the energy stored in the distribution function. They do balance for ICRH. The lost power is calculated through summating the product of the energy and weight over the lost particle population. Therefore, it provides insight into both the confinement of the particles and the lost energy. The collisional power directly implies the heating transferred to the background plasma. For NBI heating, the collisional and lost power balance shown in table 2 reflects that the differences between the low and standard mirror are not significantly large when compared to the high mirror. Furthermore, analysis of the lost power implies the improved performance of the high mirror in the overall confinement of the beam particles.

Mirror	$P_{cols}/P_{in}\%$	$P_{lost}/P_{in}\%$	Lost Particles %
High	68.5	11.8	16.2
Standard	61.2	20.2	24.7
Low	61.0	20.6	25.3

Table 2: Details of the total power transfer for the NBI heating scheme ($P_{in} = 6.84MW$).

Mirror	$P_{cols}/P_{in}\%$	$P_{lost}/P_{in}\%$	Lost Particles %
High	93.4	6.6	12.0
Standard	89.7	10.3	14.8
Low (on-ax)	81.9	18.1	13.3
Low (off-ax)	79.1	20.9	18.7

Table 3: Details of the converged power transfer for the 3-ion species ICRF scheme ($P_{in} = 1.5MW$).

Mirror	$P_{cols}/P_{in}\%$	$P_{lost}/P_{in}\%$	Lost Particles %
High	99.92	0.08	2.42
Standard	99.78	0.22	3.30
Low	99.27	0.72	3.48

Table 4: Details of the converged power transfer for the minority heating ICRF scheme ($P_{in} = 1.5MW$).

Table 3 illustrates that, despite producing highly energetic fast ion populations, the low mirror equilibrium does not transfer as much power to the background population as for the case for the high and standard mirror configurations. The small increase in lost power is due to the poor confinement of energetic particles in this low toroidal mirror magnetic geometry. For the minority heating scheme, table 4 shows improved collisional power transfer to the background species as compared to the 3-ion species scheme, as well as significantly reduced particle losses. However, an important point to note is that the RF heating simulations were made in the assumption that all the antenna power (1.5MW) is transferred to the resonant ions. Common tokamak minority heating scenarios result in 5-15% of the RF-power transferred to the background electron population through Landau damping or electron Transit Time Magnetic Pumping (eTTMP) effects.

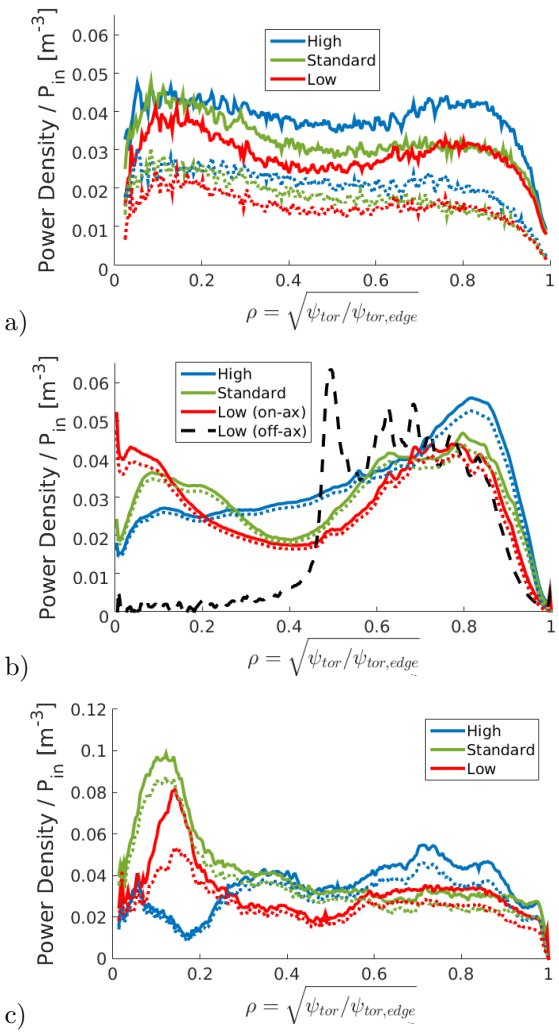

Figure 20: Radial profiles of the fast ion collisional power transfer for: a) NBI and ICRF b) 3-ion species heating and c) minority heating. Dotted lines represent the power density transferred to the background ions.

The resultant density induced by both heating methods is given in figures 8 and 17. This shows that for the high mirror all heating methods result in large particle concentrations produced at the edge. For ICRH, this issue is substantially less important than for NBI heating due to the small concentration of resonant ions. In terms of the total pressure, all equilibria for both heating systems generates core peaked values. However, for the 3-ion species scheme there is also a large edge content from the energetic trapped fast ions. Despite the peaked fast ion density content, the pressure resulting from NBI heating is not edge localised due to the percentage of the H_1 molecular ion neutral beam particles ionised in the core. Comparing this to the H_2 and H_3 molecular ions (each with a half and a third the corresponding energy respectively) which cannot penetrate as easily into the core. A crucial advantage of applying the 3-ion species scheme in the low mirror configuration is the production of highly energetic ions, reflected in figure 18). Indeed, the radial profiles of the 3-ion species heating show that localised core heating is also achieved in the low mirror. Figure 20a) shows that NBI heating results in reasonable core heating for all equilibria. The standard mirror produces weakly peaked core heating with the 3-ion species scheme, however, due to the strong toroidal dependence of the magnetic resonant surface, there is also significant edge heating. ICRF heating in the high mirror results in strongly off-axis heating at the plasma edge. Minority heating in both the low and standard mirror equilibria demonstrates strong on axis peaking. This plot does not reflect an edge-localised contribution as was seen for the cases of NBI and the 3-ion species schemes. This is due to the improved confinement of energetic particles that are core-localised. By improving the confinement of these particles, they remain in resonance for longer and thus transfer their energy to the background before being lost from the equilibrium. This explains why the collisional power density is stronger in the standard mirror than for the low mirror equilibrium, which generates significantly more highly energetic particles that are then lost and do not transfer energy to the background.

6 Summary and conclusions

This work presents the results of the simulated performance of Neutral Beam Injection and Ion Cyclotron Range of Frequency heating in different W7-X magnetic topologies. The three magnetic equilibria have different degrees of toroidal mirroring. The magnetic configurations are optimised for different properties. The high mirror is predicted to be the best performing candidate for high plasma $\langle\beta\rangle$ with respect to various qualities such as reduced bootstrap current and radial diffusion, divertor heating, etc. The standard mirror is foreseen to be the standard workhorse equilibrium used in experiments. Finally, the low mirror is an equilibrium which closely resembles the design of a classical stellarator, with the axial magnetic field strength approximately constant for all toroidal angles.

The VENUS-NBI [33] module has been updated in order to permit the calculation of neutral beam deposition in three-dimensional equilibria, and includes a realistic implementation of the W7-X NBI PINI geometry. The results show that regardless of the magnetic equilibria used, there is poor penetration of the beam into the core of the plasma for core densities above $0.25 \times 10^{20}\mathrm{m}^{-3}$.

In terms of the confinement and radial diffusion of NBI ions, the particle following VENUS-LEVIS code [13] predicts that the high mirror equilibrium has the largest particle confinement time, especially those ions located near the core. The low mirror is the worst performing magnetic topology for NBI, with the performance of the standard mirror in between high and low mirror equilibria. The final results of the NBI simulations show that the initially edge localised particles remain localised at the edge even for the full slowing down NBI distribution. This result is of considerable concern for the performance of such an auxiliary heating system.

Through the use of the SCENIC code package [9], Ion Cyclotron Resonance Heating simulations were undertaken using an antenna description radially, poloidally and toroidally localised in one of the five W7-X toroidal periods. Particular focus was given to the high-performance 3-ion species ICRF heating scheme. This requires a tailoring of the percentage concentrations of three different plasmas species with specific charge-to-mass ratios. Based on a careful choice of the particle concentrations, this heating scheme permits strong polarisation of the wave close to the wave-particle resonant surface. For the 3-ion species scheme, the predicted fast ion pressure has the largest on-axis amplitude in the low mirror equilibrium. This is due to particles remaining in resonance close to the magnetic axis for all toroidal angles. The high mirror configuration results in the lowest fast ion pressure, due to the resonant surface leaving the plasma before reaching the triangular toroidal section. Compared to the low mirror equilibrium, these lost particles do not result in a large lost power because the particles do not remain in resonance, and so lost particles have considerably lower energy values. The largest lost particle population produced through on-axis 3-ion species scheme is in the standard mirror configuration. Similar to the high mirror configuration, the toroidal displacement of the resonant surface acts to increase the particle radial diffusion. This acts to move particles into regions away from the core, resulting in confinement degradation. Due to the reduced toroidal mirror as compared to the high mirror configuration, resonant particles in the standard mirror can remain in resonance, despite the toroidal displacement of the resonant surface. This produces an increase in lost power, as the ion energies are larger and the edge confinement is worse than in the high mirror configuration. For on-axis heating, the resonant surface in the low mirror equilibrium does not displace far from the axis for different toroidal angles. This leads to improved on-axis peaking of the fast ion pressure and collisional power density for the 3-ion species and minority heating scheme compared to the standard and high mirror configurations. The low mirror configuration also produced the most energetic ion populations, with energies of up to 0.45MeV and 0.08MeV for the 3-ion species and minority heating methods respectively. The confinement of trapped energetic particles is generally poor in three-dimensional stellarator geometry. Compared to the standard mirror, 3-ion species in the low mirror results in fewer particle losses, but a larger lost power. This is a result of the improved confinement in the core due to the location of the resonant surface, but the particles that are lost have higher energies. This poor confinement of the energetic particles results in a lower transfer of power to the background plasma than for other equilibria.
For minority species heating, the lost power and lost particle percentage scales inversely with the toroidal magnetic mirror value. The minority heating scheme fails to generate the same values of highly energetic particles than the 3-ion species scheme, but results in energetic particles with improved confinement and improved collisional power transfer to the background. The transferred collisional power is a direct measure of the performance of the heating method, and the strongly on-axis collisional power peaking shown in figure 20 c) indicates that as a function of input power, the performance of minority heating for low and standard mirror equilibria leads to greatly improved core ion heating than NBI or the 3-ion species ICRF methods. ICRH in the high mirror equilibrium leads to off-axis background heating due to the trapping of resonant particles in the large toroidal magnetic well. Simulating off-axis high field side ICRH in the low mirror configuration provided insight into particle confinement in the presence of ICRH. It was seen that the fast ($v > 5v_{th}$) ion pressure is peaked over a narrow radial region $\rho \sim 0.5$, compared to a broader peaking for on-axis heating in the core (figure 17). This indicates the influence of ICRH on the radial diffusion of resonant particles.

A comparison between the slowing down NBI fast ion distribution with those of the ICRF 3-ion species and minority heating schemes was made in section 5. The three heating schemes have different merits. NBI produces large concentrations of fast ions, yet the resultant particle density profiles are strongly edge localised. This occurs for all magnetic equilibria. The 3-ion species ICRH scheme is very sensitive to the magnetic topology and the heating scheme applied. The very small concentrations of the resonant minority species results in significantly smaller pressures than that produced with NBI heating. The radial profiles of the collisional power indicate that core localised heating can be produced by both NBI and ICRF heating, but the profiles

are sensitive to the toroidal magnetic mirroring, moreso with ICRH.
Future investigations will be made into potentially combining the 3-ion species scheme with NBI heating via synergetic heating, whereby the third species would be the beam population [34]. This could also be a potential solution for strong core-localised heating performance in the high mirror equilibrium.

Acknowledgments

This work has been carried out within the framework of the EUROfusion Consortium and has received funding from the Euratom research and training programme 2014-2018 under grant agreement No 633053. The views and opinions expressed herein do not necessarily reflect those of the European Commission. The project was also supported in part by the Swiss National Science Foundation. The authors would like to thank Dirk Van Eester and Yevgen Kazakov for their advice and for all the fruitful discussions. The Piz Daint (CSCS, Switzerland) and the MARCONI-Fusion (CINECA/ENEA, Italy) supercomputer facilities were used for the simulations presented in this research. Numerical calculations using Piz Daint were supported by a grant from the Swiss National Supercomputing Centre (CSCS) under project ID 's743'. The SCientific IT and Application Support (SCITAS) centre based at EPFL is also acknowledged for the help with on-site computer support.

References

[1] Thomas H Stix. *Waves in plasmas*. Springer Science & Business Media, 1992.

[2] T. Andreeva et al. *Prob. of Atom. Sci. Cent.*, 4:R45–R47, 2002.

[3] M. Drevlak et al. *Nuc. Fus.*, 54(073002), 2014.

[4] J.M. Faustin et al. *Nuc. Fus.*, 56(9):092006, 2016.

[5] J. M. Faustin et al. *Plas. Phys. Cont. Fus.*, 58(7):074004, 2016.

[6] Y. O. Kazakov et al. *Nuc. Fus.*, 55:032001, 2015.

[7] Y. O. Kazakov et al. *Nat. Phys.*, 13:973–978, 2017.

[8] J. M. Faustin et al. *Plas. Phys. Contr. Fusion*, 59:084001, 2017.

[9] M. Jucker et al. *Comp. Phys. Comm.*, 182(912-925), 2011.

[10] W.A. Cooper et al. *Comp. Phys. Comm.*, 180(9):1524–1533, 2009.

[11] M. Albergante. *Interaction between fast ions and microturbulence in thermonuclear devices*. PhD thesis, École Polytechnique Fédérale de Lausanne, 2011.

[12] N. Mellet et al. *Comp. Phys. Comm.*, 182:570, 2011.

[13] D. Pfefferlé et al. *Comp. Phys. Comms.*, 185(12):3127 – 3140, 2014.

[14] M. Greenwald. *Plasm. Phys. Cont. Fus.*, 44:R27–R80, 2002.

[15] H.S. Bosch et al. *Contrib. Plas. Phys.*, 50(8), 2010.

[16] S. P. Hirschman et al. *Plas. Fluids*, 26(12):3553, 1983.

[17] Y. Turkin et al. *Phys. Plas.*, 18:022505, 2011.

[18] C.D. Beidler et al. *Nuc. Fus.*, 51(7):076001, 2011.

[19] S.P. Hirshman et al. *Phys. Fluids*, 29(9):2951–2959, 1986.

[20] Y. Turkin et al. *Fus. Sci Tech.*, 50(3):387–394, 2006.

[21] J. Faustin. *Self-Consistent Interaction of Fast Particles and ICRF Waves in 3D Applications of Fusion Plasma Devices*. PhD thesis, École Polytechnique Fédérale de Lausanne, 2017.

[22] Robert G. Littlejohn. Variational principles of guiding centre motion. *J. Plasma Physics*, 29(1):111–125, 1983.

[23] John Wesson and DJ Campbell. *Tokamaks*, volume 149. Oxford University Press, 2011.

[24] R. Koch. *Fus. Sci. Tech.*, 49:167–176, 2006.

[25] D. Cohen-Or and A. Kaufman. *Graphical Models and Image Processing*, 57(6):453–461, 1995.

[26] O. Asunta et al. *Comp. Phys. Comm.*, 188, 2015.

[27] A. Pankin et al. *Comp. Phys. Comms.*, 159(3):157 – 184, 2004.

[28] M. McMillan and S. A. Lazerson. *Plas. Phys. Cont. Fus.*, 2014.

[29] P. Helander. *Rep. Prog. Phys.*, 77(087001), 2014.

[30] H. E. Mynick. *Phys. Plas.*, 13, 2006.

[31] J. Ongena et al. *Phys. Plas.*, 21(6):061514, 2014.

[32] T. H. Stix. *Nuclear Fusion*, 15(5), 1975.

[33] D. Pfefferlé, J.P. Graves, W.A. Cooper, C. Misev, I.T. Chapman, M. Turnyanskiy, and S. Sangaroon. Nbi fast ion confinement in the helical core of mast hybrid-like plasmas. *Nuclear Fusion*, 54(6):064020, 2014.

[34] J. Ongena et al. *EPJ Web. Conf.*, 157:02006, 2017.